Lab on a Chip

ROYAL SOCIETY OF CHEMISTRY

PAPER

View Article Online
View Journal | View Issue

Check for updates

Cite this: *Lab Chip*, 2023, **23**, 3258

Received 11th April 2023,
Accepted 20th June 2023

DOI: 10.1039/d3lc00312d

rsc.li/loc

Acoustofluidic large-scale mixing for enhanced microfluidic immunostaining for tissue diagnostics†

Muaz S. Draz, *[a,b] Diego Dupouy[b] and Martin A. M. Gijs[a]

The usage of microfluidics for automated and fast immunoassays has gained a lot of interest in the last decades. This integration comes with certain challenges, like the reconciliation of laminar flow patterns of micro-scale systems with diffusion-limited mass transport. Several methods have been investigated to enhance microfluidic mixing in microsystems, including acoustic-based fluidic streaming. Here, we report both by numerical simulation and experiments on the beneficiary effect of acoustic agitation on the uniformity of immunostaining in large-size and thin microfluidic chambers. Moreover, we investigate by numerical simulation the impact of reducing the incubation times and the concentrations of the biochemical detection reagents on the obtained immunoassay signal. Finally, acoustofluidic mixing was successfully used to reduce by 80% the incubation time of the Her2 (human epidermal growth factor receptor 2) and CK (cytokeratins) biomarkers for the spatial immunostaining of breast cancer cell pellets, or reducing their concentration by 66% and achieving a higher signal-to-background ratio than comparable spatially resolved immunostaining with static incubation.

Introduction

Microfluidics has been very promising for use in many scientific and engineering fields, such as medical diagnostics and biochemical analytics,[1–3] chemical synthesis,[4] drug development,[5] forensics analysis,[6] energy applications,[7] and environmental monitoring.[8] This has been facilitated by diverse assets that microfluidics offer such as a reduced device size, a reduced sample volume required, a lower associated cost of analysis, a reduction in the time of experimentation, and high-throughput and automation.[9–13] The application of microfluidics in the field of spatial molecular profiling of tumor tissues has gained a lot of interest in the last years,[14–17] especially with the increased interest in personalized medicine and targeted therapy. Simply, a dissected thin tissue section of the tumor is mounted on a substrate slide (*e.g.*, a glass slide) and incubated inside a chamber with controlled fluid flow and temperature, and different specific detection reagents such as antibodies, or DNA oligos can be used to target the marker(s) of interest, followed by subsequent visualization with microscopic techniques (fluorescence or chromogenic bright-field). This allows for detecting the presence and the level of expression of such markers. The two most common techniques for tissue diagnostics are immunohistochemistry (IHC) and *in situ* hybridization (ISH),[18,19] where in the former the expression of certain protein markers in a cell population can be detected, and in the latter, a labeled RNA or DNA probe can be used to study the gene expression in the cellular environment. Three important factors affect the performance and the quality of these diagnostic techniques using microfluidic systems, namely, the uniformity of the tissue staining, the used detection reagent concentration, and the incubation times onto the tissue. The uniform staining of the tissue plays an important role in the analysis since it ensures that all relevant target analytes on the tissue are exposed equally to the detection reagents, enhancing the signal contrast and leading to consistent results.[20] Non-uniform staining might jeopardize the analysis of the tumor section, leading to a false or biased diagnosis or prognosis.[16,19,21] There have been several reports on the adaption of a microfluidic tissue processor system (MTP) for tissue immunostaining,[14–16,19,22–26] where the thin tissue section is mounted on a glass slide and incubated inside a chamber where a microfluidic distributing channel network is used to distribute the bioreagents uniformly above the tissue. The same concept of the distribution channel network has been adopted for other research purposes such as in the microfluidic concentration gradient generator,[27–30] where the common characteristic of these designs is the possibility to

---

[a] Laboratory of Microsystems 2, Ecole Polytechnique Fédérale de Lausanne (EPFL), CH-1015 Lausanne, Switzerland. E-mail: muaz.draz@epfl.ch

[b] Lunaphore Technologies SA, CH-1131 Tolochenaz, Switzerland

† Electronic supplementary information (ESI) available. See DOI: **https://doi.org/10.1039/d3lc00312d**

generate a concentration gradient across the channel width and perpendicular to the flow direction. This concentration gradient can be beneficial for chemotaxis studies, in which chemicals need to be delivered to cells in a concentration-gradient form,[31] and for optimized neural stem cells growth and differentiation,[32] and for yeast gene expression under gradients of pheromones,[33] or for gradient treatments of cells across the width of the microchannel.[34] However, these gradients can have the disadvantageous effect of the uneven staining of the tissue. The concentration gradients can be minimized in tissue staining, including by applying extremely high-pressure microfluidics to induce turbulent reagent streams, by lowering the distance between the neighboring streams in the microfluidic channel distribution network (which can be limited with the maximum pressure the system can withstand), or by prolonging the reagent's incubation time to allow for the reagents to diffuse. The use of high pressure in microfluidic systems would require high-pressure pumps, and the firm sealing of the fluidic chamber; otherwise fluid leakage might happen during the experiments leading to non-proper functioning and possible safety concerns.[19,35,36] At the same time, high flow rates can lead to high frictional shear forces acting on the surface-mounted cells thus affecting their cellular function and biological responses,[37,38] and can affect the tissue morphology and integrity. Moreover, high flow rates running through relatively small diameter inlet holes and along sharp edges can lead to cavitation microbubble,[39,40] which, if trapped inside the chamber, can alter the flow dynamics and the exposure of the tissue sample to the detection reagents. Secondly, reducing the incubation times of immune detection reagents with the tissue can be of vital benefit, since this can shorten the analysis time and thus provide faster results. Moreover, it can reduce the background signal due to nonspecific binding.[19,21,41] However, reducing the incubation time would mean shorter exposure periods are given to the detection reagents to interact with the target tissue, reducing the immunostaining signal. In addition to that, during the incubation time, a depletion region with a low concentration of the reagents is formed above the reacting surface (tissue), whereafter the immuno-reaction starts to be diffusion-limited.[42,43] Biological molecules having diffusion coefficients in the range of 10^{-11} to $(10^{-12}$ m^2 s$^{-1})$[44,45] would need longer incubation times to be able to diffuse throughout the chamber and interact with the tissue. Finally, the concentration of the immunoreagents can have a great impact on the immunoassays since reducing the consumption of the bio-reagents can reduce the overall cost of the experimental and diagnostic tests. Additionally, high concentrations of antibodies used for immunohistochemistry can lead to false positives or excessive background staining,[46,47] and it is frequently found that many antibody production companies suggest the reduction of the antibody concentration to reduce the nonspecific binding. On the other hand, reducing the concentration of the reagent would lower the amount of the available detection reagents above the tissue and thus reduce the immunodetection signal. The impact of the low concentration on the detection signal is larger when it is considered with the abovementioned depletion region formation and the limited diffusional mass transport of the bio-reagents. Several technologies have been developed and integrated into microfluidics to induce a disruption between the fluid thin layers associated with the laminar flow regime by enhancing the fluidic mixing and thus helping to counteract the diffusion-limited transport of the bio-chemical reagents in microfluidic systems. For example, magnetic-based microfluidic mixing was investigated where a fluid of dispersed magnetic particles or rods inside the chamber is actuated by an external magnet,[48,49] but this requires a closely attached magnetic actuator and the magnetic beads can interfere with the immunoassay performance while limiting the optical readout through the chamber. Moreover, acoustic actuation of embedded microstructures,[50–52] vibrating structures[53,54] or trapped microbubbles[55,56] has been investigated for microfluidic mixing which can require a lengthy microfabrication process, and the efficient trapping of the microbubbles inside the chamber throughout the full experiment, and possibly the need for high-frequency matching and signal generators.[57] Furthermore, electro-kinetic techniques such as the AC-electrothermal technique have been used for enhancing the microfluidic mixing and immunoassays, but it requires the microfabrication of the actuating electrodes and, if not optimized, can generate relatively high temperatures and lead to electrolysis.[43,58,59]

Here we introduce the integration of a low-frequency acoustofluidic mixing device for enhancing microfluidic immunostaining. Piezoelectric actuators are mounted with water-soluble glue on the exterior surface of a microfluidic staining system and the actuation of the piezoelectric elements leads to the generation of vortex-like patterns of acoustic streaming within the microfluidic chamber. The proposed idea has several advantages, including ease of integration, working at low frequencies thus omitting the need for advanced and accurate high-frequency devices, a low cost of the core element (our piezoelectric actuator costs less than 1 USD), the absence of any microfabrication steps and retaining the possibility of microscopic imaging over the complete thin chamber, and, finally, the absence of thermal interference with the conducted experiments. We performed a preliminary investigation by the numerical simulation to explain the working mechanism behind the reported work, including the investigation of the effect of the piezoelectric element actuation on the system vibration and more specifically at the solid–fluid interface. The simulated acoustic pressure and solid mechanical stress are then coupled to the fluidic domain to investigate acoustic streaming and the associated microparticle motion. The presence of acoustofluidic vortex-like patterns was then validated by the experimental tracing of fluorescence microparticles. Acoustofluidic mixing was investigated for its potential with respect to the immunostaining performance (elimination of non-uniform staining due to microfluidic gradients, reducing the reagents' incubation times, and enabling the use of lower reagent concentrations). Furthermore, numerical simulation was used to investigate the formation of the concentration depletion region above a reacting surface and the associated rapidly decaying reaction rate, and the effect of using lower reagent concentration on the surface reaction. Finally, we demonstrate the feasibility of using the acoustofluidic mixing to enhance the immunostaining of several antibodies with different molecular weights such as the Her2 tumor marker (human epidermal growth factor receptor2, also known as ERBB2) and CK (cytokeratins) antibodies cocktail on Bt-474 cancer cell pellet sections. The Her2 gene is amplified in 18–20% of the primary breast cancer cases, leading to the overexpression of the associated protein, rapid tumor proliferation, and poor prognosis of the disease.[60] CK has been widely used in the histopathological evaluation of breast carcinoma to identify tumor epithelial cells and help in differentiating between the specific breast cancer subtypes.[61] To the best of our knowledge, this is the first research that demonstrates acoustofluidic mixing for immunostaining on cell pellet sections, and we believe this can be also applied for more accurate and enhanced spatial proteomic and transcriptomic analysis. The experimental acoustofluidic mixing device was successfully used, and in contrary to the results that might be anticipated based on the simulation of static incubation of surface reactions, to reduce the reagents incubation time by 80% and reducing the reagents consumption by 66%, while still obtaining higher signals than a static incubation.

Experimental setup

The experimental setup relies on a wide and thin microfluidic system that has been used before for tissue diagnostics.[15,16,19,22–26] The core element is a polymer chip (Fig. 1a) which provides the fluidic connections to the chamber (through the small white inlet holes). The latter has a glass coverslip at its top, which allows for imaging accessibility. The staining chamber is realised by clamping the polymer chip against the substrate slide that carries a tissue or cell pellet slice and being in contact with a bottom temperature-controlling system (Fig. 1b). An O-ring (Fig. 1b) is used to ensure chamber sealing and prevent fluidic leakage. Two piezoelectric transducers (RND 430-00018) (Fig. 1) are glued on the exterior face of the stainer top plate and aligned horizontally with the microfluidic chamber. A water-based glue (Tensive conductive adhesive gel) was used which allows the easy positioning and re-application of the transducers. The piezoelectric transducers are actuated with a function generator (AFG3021B, Tektronix), and the signal is amplified with a high voltage amplifier (WMA-300, Falco-system) and monitored by an oscilloscope (54602B, HP). The transducer located to the left of the chamber is actuated at

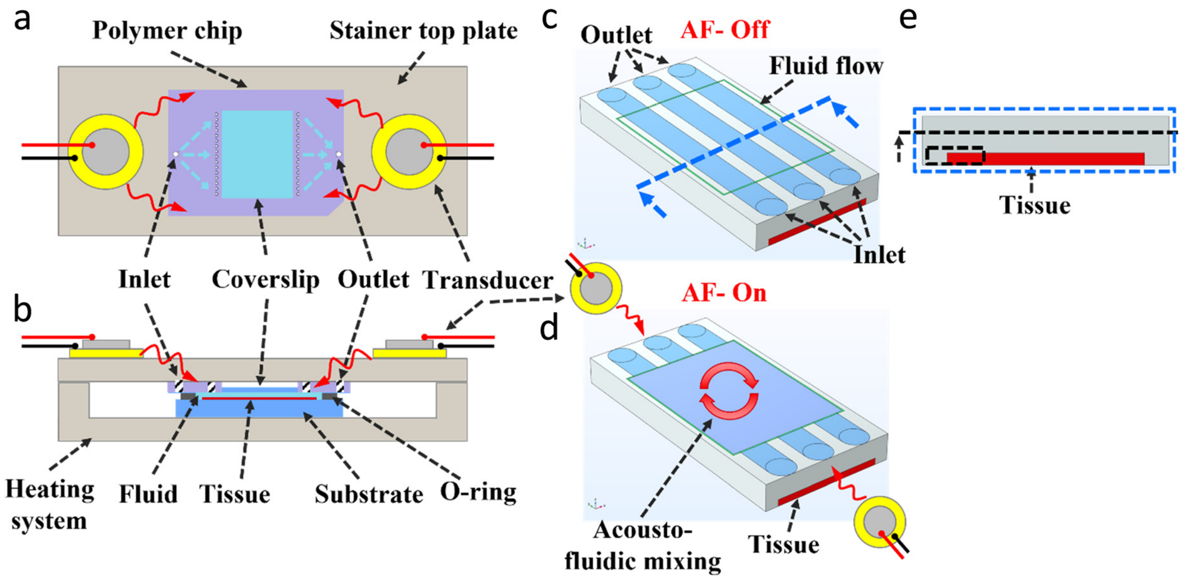

Fig. 1 Experimental setup. (a) Top schematic view of the microfluidic setup with the piezoelectric transducers mounted on the two sides of the stainer top plate, and the polymer chip used with the distributed channel network design (the larger white inlet hole supplying the fluid into the multiple fluidic paths represented by the blue dashed arrows to dispense the liquid into the chamber through the small white holes, and similar for the outlet). A glass coverslip is located at the polymer chip centre which allows imaging accessibility from the top. (b) Cross-sectional schematic side view of the closed system setup showing the polymer chip clamped against the substrate holding the sample (*e.g.*, a tissue) with an O-ring that seals the microfluidic chamber ($15 \times 15 \times 0.05$ mm^3). A heating system is used to control the temperature of the setup. (c and d) Simplified schematic of the acoustofluidic mixing within a part of the microfluidic chamber, showing three inlet/outlet ports, and a thin tissue located at the chamber bottom, before (c) and after (d) actuating the piezoelectric transducers. (e) Front view image of the chamber (at the cross-section line of Fig. 1(c)), with the thin tissue located at the bottom, and a cross-sectional dash-line and dash-line box showing the region considered for further analysis in Fig. 4–6.

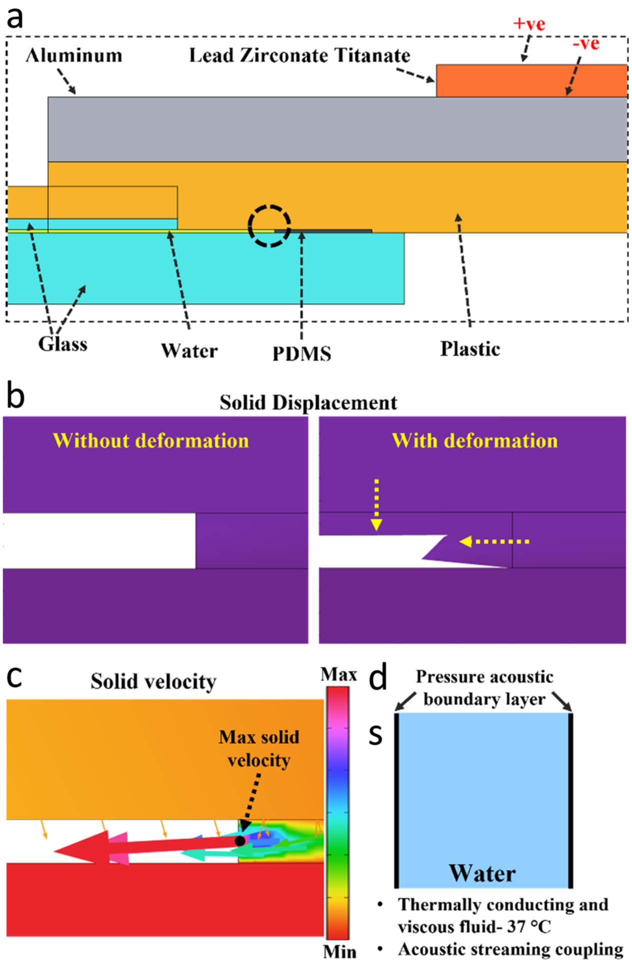

Fig. 2 Acoustofluidic simulation. (a) The components used in the 2D setup (side view) for the characterization of the acoustic vibration and solid mechanics of the system. A transducer (lead zirconate titanate, PZT) is actuated by the AC signal (+ve and −ve) and mounted on the top of a metallic (aluminium) plate which is clamped against the polymer (plastic) chip, and the glass coverslip and glass substrate, and the water chamber sealed from the side with a PDMS ring. (b) The solid displacement of the system at the region of interest (ROI) is indicated by the dash-circle in Fig. 2a as a result of the actuation of the PZT transducer. The solid deformation shows the displacement of the plastic and PDMS domains. (c) The solid velocity at the same ROI showing the maximum velocity point is located at the PDMS–water interface boundary, and the arrows show the solid velocity direction with the arrows' size proportional to the solid velocity components (*X*, *Y*). (d) The 2D setup (top view) that is used for the characterization of the pressure acoustics and the fluid flow and particles' tracing, taking the side walls as vibrating boundaries as obtained from the 2D simulation in Fig. 2c.

6.5 kHz and 18 mArms while the transducer located to the right of the chamber is actuated at 5.4 kHz and 18 mArms throughout the whole presented work. The frequencies were selected to provide the maximum fluid velocity observed by the fluorescent microparticles, while the acoustic power was selected to provide a strong and homogeneous immunostaining of the incubated tissue/cells. For each experiment with acoustofluidic mixing, the experiment duration was divided into four-time slots, and the two transducers were actuated sequentially (*e.g.*, for the 4 minutes experiments, the 1st minute: right PZT-on and left PZT-off, then for the 2nd minute: right PZT-off and left PZT-on, …*etc.*). All fluid handling and flow rates were controlled by an integrated pressure pumping system. Fig. 1c shows a simplified schematic section of the core of the microfluidic chamber (showing here only 3 inlet/outlet ports, while the actual chip has multiple of inlets/outlets) that allows dispensing laminar flow streams of the reagents from the small holes over the thin tissue located at the bottom of the chamber. Fig. 1d shows a simplified schematic of the acoustofluidic mixing patterns generated after the actuation of the piezoelectric transducers located at the sides of the chamber. All details of the immunoassay and fluorescence imaging are described in the ESI† (ESI protocols). The temperature generated by the transducers was monitored by a thermal IR camera and the results (ESI† Fig. S1) showed no change in the temperature due to the actuation of the piezoelectric transducers.

Numerical simulations

Surface-based reaction and microfluidic analyte transport

It is presumed that the reaction between the diffusing reagent analyte and the surface-immobilized target (tissue) will proceed according to a first-order Langmuir adsorption model.[62] Eqn (1) relates the target density B_0 to the reagent analyte concentration at the reaction surface A_{surface} and the molar concentration of the analyte–target complex $[AB]$ being generated over the reaction time,[43]

$$\frac{\partial [AB]}{\partial t} = k_{\text{on}}[A]_{\text{surface}}\,\{[B_0]-[AB]\} - k_{\text{d}}[AB] \qquad (1)$$

where k_{on}, k_{d} are the association and dissociation rate constants respectively. The initial target density used is B_0 = 3.3 × 10^{-8} [mol m^{-2}], and the reagent dissociation constant k_{d} = 10^{-2} [1 s^{-1}], and the reagent association constant k_{on} was simulated for the value of k_{on} = 10^{6} [m^{3} s^{-1} mol^{-1}], all simulations were done by COMSOL Multiphysics 6.0. The initial bulk reagent analyte concentration A_{surface} available at the reacting surface (tissue) was simulated for the range of 10^{-10}, 0.5 × 10^{-10}, 0.33 × 10^{-10}, and 0.25 × 10^{-10} (mol m^{-3}). The reagent bulk concentration over the reacting surface tissue can be replenished by the fluid flow according to Fick's second law of diffusion, as shown in eqn (2),[43]

$$\frac{\partial [A]}{\partial t} + U{\cdot}\nabla[A] = D\,\nabla^2[A] + R \qquad (2)$$

where A is the reagent analyte concentration in the bulk fluid, U is the fluid flow velocity, D is the reagent analyte's diffusion coefficient, and R is the reaction rate, which in the bulk fluid equals zero given that there is no reaction occurring in the fluid.

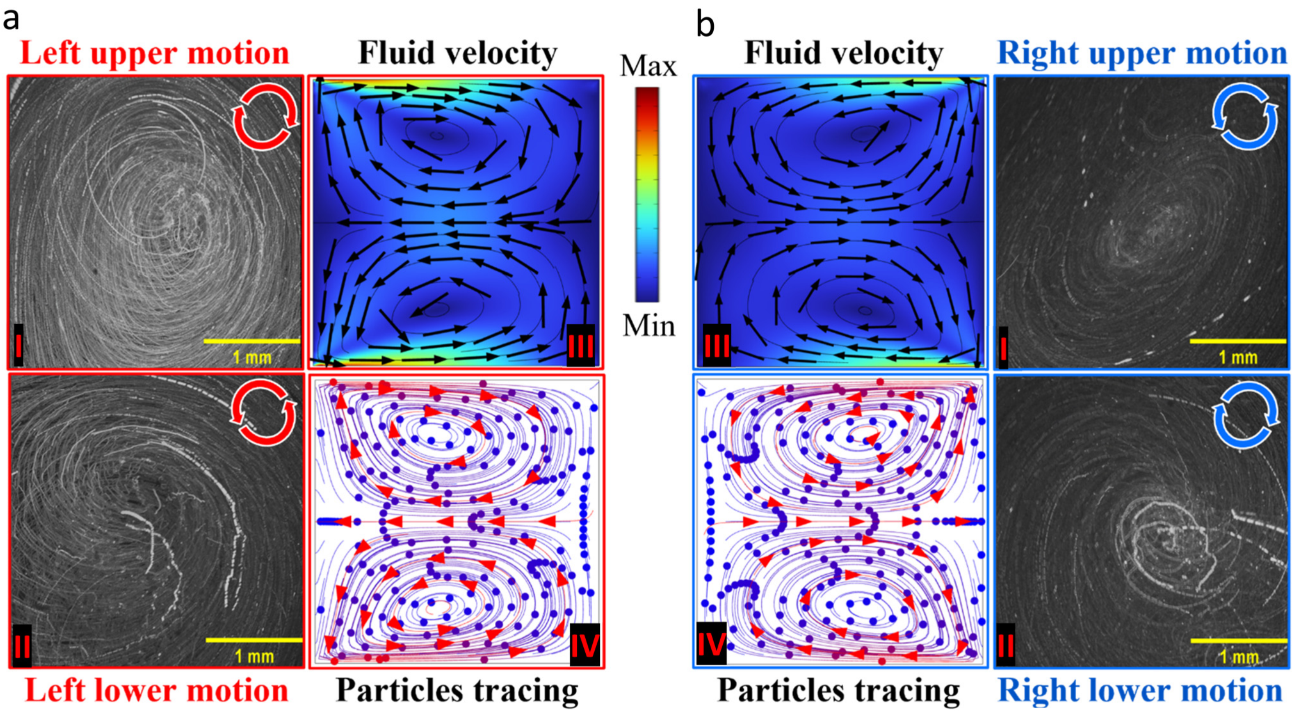

Fig. 3 Acoustofluidic mixing. (a) and (b) show the experimental (I and II) and the simulation (III and IV) results of the acoustofluidic motion generated after the activation of the piezoelectric transducers, positioned to the left (a) or to the right (b) of the microfluidic chamber, as shown in Fig. 1(a). The left and the right transducer were actuated at the frequencies of 6.5 and 5.4 kHz, respectively, each generating two vortex-like patterns of fluidic motion. Sub-figures (I and II) show the experimental superimposed images of fluorescent microparticles observed at the top (I) and the bottom (II) parts of the chamber. The red and blue arrows indicate the observed acoustofluidic motion direction when the left (red) or the right (blue) transducers were activated. Sub-figures (III and IV) show the microfluidic fluidic motion direction (III) and the microparticles (3 μm) tracing (IV) in the square chamber, resulting from the actuation of each of the side boundary layers. The simulation was carried out according to the model shown in Fig. 2(d) and as described after. Both figures show two fluidic vortices that are similar in fluid direction to those observed in sub-figures (I and II) at the top and bottom of the chamber.

Acoustofluidics

The numerical simulation (using COMSOL 6.1) of the acoustofluidic motion was done in two steps. In the first part, the setup in 2D from the side view was simulated to gain insights into the effect of the transducer actuation and the accompanying acoustic pressure distribution, and the solid stress and strain (Fig. S3b†). The electrostatic module was used to actuate the transducer (lead zirconate titanate, PZT) by applying an AC signal as shown in Fig. 2a, and the solid mechanics module was used to compute the solid components' structural analysis. The PZT material was used in the stress-charge form using the PZT-4D properties. Finally, the pressure acoustics module was simulated to compute the pressure variation and the acoustic wave propagation into the fluid. All three modules were solved in the frequency domain and the piezoelectric effect was used to couple the electrostatics and solid mechanics physics, while the acoustic-structure boundary was used to couple the pressure acoustics and the structural components of the system, as shown in ESI† (Fig. S3a). Fig. 2b shows the solid displacement at the region of interest (ROI) (indicated by a dashed circle in Fig. 2a), which is situated at the first contact point (close to the PZT) between the solid components and the fluid domain. The system deformation at that region shows the displacement of the plastic and PDMS domains (soft materials,[63,64]) as a result of the transducer actuation. Furthermore, the solid velocity as a result of the acoustic structural boundary coupling was computed which takes into account the fluid load on the structure and the structural acceleration as experienced by the fluid. Fig. 2c shows that the maximum solid velocity point of the whole simulated setup is located at the boundary layer of the PDMS–water interface, while the colored arrows show that the solid velocity components in the x (lateral) direction are the highest. Both the solid displacement and velocity are scalable with the applied acoustic power, and thus higher actuation (higher voltages) would lead to higher velocities (ESI† Fig. S5). In the second 2D simulation, the fluid domain from the top view, as shown in Fig. 2d, with the side acoustic boundary layers was used to simulate the pressure variations and the propagation of acoustic waves and the resulting acoustofluidic motion, as described in the ESI† (Fig. S3b). The pressure acoustics module was used, where a thermoviscous acoustic boundary layer is applied to the right or the left side of the fluid chamber. A mechanical wall vibration was used taking into account the range of wall displacements[65–67] computed in the first

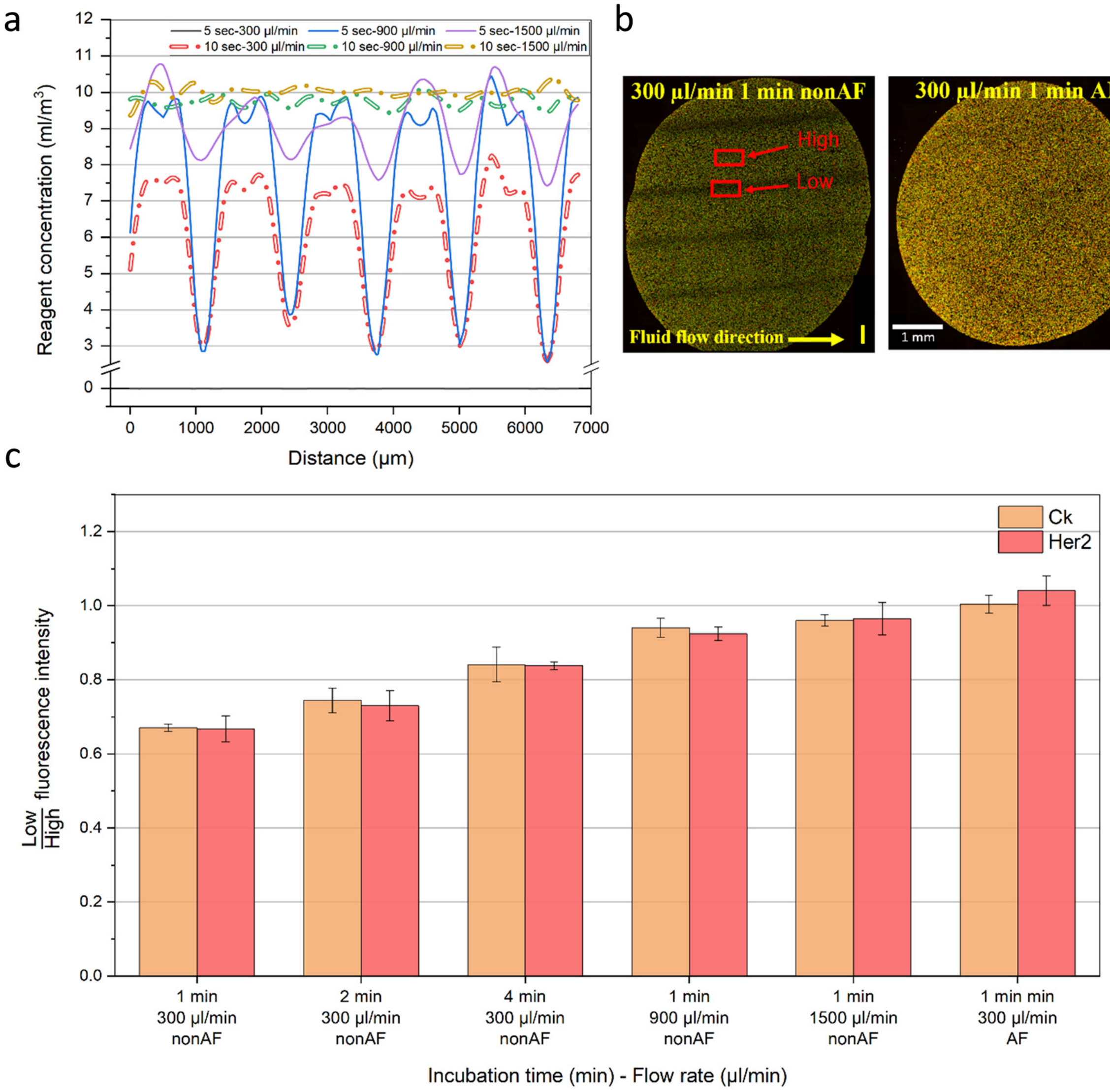

Fig. 4 Smoothening of microfluidic gradients by acoustofluidics. (a) The reagent concentration (mol m^{-3}) (at the middle of the chamber as indicated by the cross-sectional dashed line in Fig. 1c and across the middle of the chamber height, as indicated by the cross-sectional dashed line in Fig. 1e), for three fluidic flow rates 300, 900, and 1500 μl min^{-1} after 5 and 10 seconds, obtained by numerical simulation. (b) Fluorescence images of a Bt-474 cancer cell pellet stained with Her2 marker (green) and CK marker (red) at a 300 μl min^{-1} dispense flow rate, followed by an incubation time of 1 min, without (I) and with (II) the acoustofluidic mixing. (c) Analysis of the experimental microfluidic staining gradients (ratio of the lowest over the highest fluorescent intensity). Different flow rates and incubation times were used (300 μl min^{-1} for 1, 2, and 4 min incubation time and 900 and 1500 μl min^{-1} for 1 min incubation time), all without acoustofluidic mixing, and finally 300 μl min^{-1} with 1 min incubation time with acoustofluidic mixing showing the absence of the staining gradients.

part, with a velocity $V_{\text{wall}} = D_0\omega$ (m s^{-1}) where D_0 is the displacement magnitude and ω is the angular frequency. The fluid domain was assumed to be thermally conducting and viscous to take into account the attenuation due to bulk viscous losses. Due to the acoustic wave attenuation and the generated gradients in the time-averaged acoustic momentum flux in a viscous fluid, a net displacement of the fluid particles is generated leading to a steady fluid flow known as acoustic streaming.[68–70] For fluids and assuming that the pressure varies harmonically in time, the acoustic field pressure can be described according to eqn (3),

$$\nabla\cdot\left(-\frac{1}{\rho_c}\nabla p\right)-\frac{w^2 p}{c^2\rho_c}=0 \tag{3}$$

where p is the pressure (Pa), ρ_c is the density (kg m^{-3}), c is the speed of sound (m s^{-1}), and w is the angular frequency of the pressure field. After solving for the acoustic pressure and the sound levels and the acoustic acceleration in the system, the output was coupled to the laminar flow module, where the pressure and velocity fields of the time-average fluid flow using the Navier–Stokes equations were computed. Finally, the time-averaged Stokes drag force (F_{drag}) on spherical particles with radius (r_p) and moving with a velocity (u) while being located inside a viscous fluid with a streaming velocity (v) can be calculated by eqn (4),[67]

$$F_{\text{drag}} = 6\pi\mu r_p(v - u) \tag{4}$$

where μ is the dynamic viscosity of the fluid (Pa s).

Results & discussion

Acoustofluidic mixing

When the piezoelectric transducers located at the sides of the experimental setup shown in Fig. 1 and 2a are actuated, the device resonates. Since the device components are firmly clamped against each other, the resonation of the transducer is translated throughout the device, depending on several factors including the speed and attenuation of sound on each material component. Since most of the setup components are firmly fixed against each other and the surrounding device and are highly sealed to ensure no leakage during the experiments, an analysis of the resulting acoustic pressure distribution and the solid mechanics shows that the inner sides of the polymer chip facing the fluidic chamber possess the highest vibration amplitude, as shown in Fig. 2b and c. This is mainly because the sidewalls made of PDMS are the softest material (with the highest vibration amplitude) used in the system. Since these elements are in direct contact with the fluid, their vibration would lead to the agitation of the fluid and the generation of the acoustofluidic motion. Fig. 3a and b show the experimental and numerical simulation results of the acoustofluidic motion observed in the chamber under the actuation of the left transducer (Fig. 3a) at 6.5 kHz or the right transducer (Fig. 3b) at 5.4 kHz. This range of frequencies was found to generate the strongest microfluidic motion, as observed by the tracing of the fluorescence microparticles. The difference in the frequencies can be due to the non-symmetrical shape of the system components such as the polymer chip and the location where the chip is mounted in the system. Generally, in each case, two large-scale vortex-like patterns of acoustic streaming were observed at the top and bottom regions of the chamber with opposite directions of motion. Fig. 3a-I and -II and b-I and -II show the superimposed images of the fluorescence microparticles when the left (Fig. 3a) or the right (Fig. 3b) transducer was actuated. The direction of the fluid motion is generally pointing horizontally away from the actuated transducer and away from the close upper and lower corners of the chamber. ESI† Videos S1 and S2 show two regions showing vortex-like fluid motion indeed, as observed for actuating the transducer located to the right of the chamber at 5.4 kHz (Video S1†) or to the left at 6.5 kHz (Video S2†), where several sizes of fluorescent microparticles (4, 4.96, 8.87, 10.14 μm) were tested. We have noted that some particles tend to aggregate over time, even before applying the acoustic field, probably due to particle-particle interactions.[71] Moreover, some particles under the effect of the acoustic field, showed a circular motion while following the large acoustofluidic vortices. This can be due to the viscous torque as a result of the acoustic streaming in the viscous boundary layer around the particle itself or the acoustic torque induced on the object.[72–74] Fig. 3a-III and b-III show the numerical simulation results (full chamber) of the fluid vortices (two vortices for each transducer) under the actuation of the left (a) or the right (b) sides of the chamber (shown in Fig. 2d) as a pressure acoustic boundary layer. The simulated domain is filled with water at 37 °C and assumed to be a thermally conducting and viscous fluid while the acoustic streaming is coupled from the pressure acoustics to the fluid domain and its borders. The acoustic pressure of the fluidic chamber is shown in ESI† (Fig. S4). For each of the actuated side transducers, the numerical simulation shows two acoustofluidic motion areas with vortex like-pattern in the chamber, where the fluid direction of motion agrees with the experimentally observed acoustofluidic vortex-like patterns (shown in Fig. 3a-I and -II and b-I and -II) and the ESI† Videos (S1 and S2). Carrying out the numerical simulation while coupling only the acoustic pressure to the boundary layer and disabling the domain coupling, shows the same results and velocity values. This indicates that the major mechanism behind the acoustic streaming is linked to the PDMS boundary layers, and not the effect of the acoustic pressure acting as a volume force on the bulk fluidic. Fig. 3a-IV and b-IV show the numerical simulation results of the microparticles tracing under the effect of the fluid Stokes drag force calculated using eqn (4). The microparticles are initially dispersed uniformly throughout the full chamber. However, under the effect of the acoustofluidic generated motion, the microparticles follow the fluidic streamlines, as shown in the ESI† Video S3. Similarly, the microparticles' direction of motion agrees with the experimentally observed microparticle motion shown in Fig. 3-I and -II and the ESI† Videos S1 and S2. The simulated microparticles size was 3 μm, however, a wide range of microparticle sizes was tested and was all found to follow the acoustofluidic vortices direction with expected differences in the particle's velocity. Finally, the microparticles can be affected by the acoustic radiation forces which can move and focus the microparticles in the pressure nodes based on their acoustic contrast to the surrounding fluid.[75] However, given the frequencies in the low sub-MHz regime used in the current research (6.5 and 5.4 kHz), the streaming-induced velocity tends to be much higher than the acoustic radiation forces.[67,76]

Acoustofluidic smoothening of microfluidic gradients

Here, we show how acoustofluidics help smoothening the microfluidic gradients that can be formed inside the chamber due to the laminar flow regime of the fluid and the microfluidic channel network design used, thereby leading to more uniform staining within the thin chamber. Fig. 4a shows the cross-sectional numerical analysis of the analyte reagent concentration (mol m^{-3}) at the chamber center as indicated by the cross-sectional dash line in Fig. 1e, at three different fluidic flow rates of 300, 900, and 1500 μl min^{-1}, after 5 and 10 s of fluid dispensing, obtained by simulation. The high-concentration peaks correspond to the locations in front of the inlet/outlet ports (blue wide lines in schematic Fig. 1c), while the low-concentration peaks correspond to the locations in between the side-by-side inlet/outlet ports (white wide lines in schematic Fig. 1c), where the fluid velocity is lower. This evidently leads to big differences in the available reagent concentrations above the adjacent tissue slices horizontally along the chamber width. The average ratio (n = 10) of the concentration minima over the peak concentrations along the line in Fig. 1e, after 5 and 10 s, is 0.09% and 45% for 300 μl min^{-1}, and 26% and 98% for 900 μl min^{-1}, and 69% and 100% for 1500 μl min^{-1}, respectively. It is worth noting that the tissue is experiencing these concentration differences during the active bioreagent dispensing, where a very fast replenishment of the reacting species is happening above the tissue. These differences at such fluid velocities, even if happening for a short time, can lead to big differences in the bioreagents distribution and thus lead to the non-uniform staining of the tissue sample and possibly a false diagnostic analysis of the biological marker of interest. Fig. 4b shows the experimental staining of a large Bt-474 (human breast cancer tissue) section with 300 μl min^{-1} dispense flow rate and 1 min incubation time of primary antibodies (Her2 rabbit and CK mouse) and secondary antibodies (anti-rabbit 647 and anti-mouse 555) all at 1:200 dilution ratio, without (I) and with (II) the acoustofluidic mixing. The full immunostaining protocol is described in the ESI.† After the immunoassay, the sections were mounted and imaged using an automatic fluorescent scanning system, and the fluorescence intensity was measured as explained in the ESI.† Fig. 4b-I shows a clear non-homogenous gradient staining of the section with the two markers used (Her2 in green color and cytokeratins in red color), where the direction of the gradients is perpendicular to the fluid flow direction and the multi-inlet/outlet ports. Fig. 4b-II shows the effect of the acoustofluidic mixing on the active uniform distribution of the bioreagents over the tissue and throughout the chamber thus the elimination of the gradients overserved. The effect is indicated in schematic Fig. 1d: acoustofluidic mixing will induce a large-scale transversal motion that disrupts the laminar flow streams and induces the mixing perpendicularly between the long flow lines. Fig. 4c shows the statistical analysis of experimental microfluidic gradients experienced by the Bt-474 sections at a flow rate of 300 μl min^{-1} after 1, 2, and 4 min of each antibody incubation time, and 900 and 1500 μl min^{-1} after 1 min of antibodies incubation time, without the acoustofluidic mixing. In all cases, a similar and large volume of 350 μl of each antibody was dispensed to ensure a full filling of the fluidic tubes and the microfluidic chamber. The low and high fluorescence intensities are measured at the Bt-474 sections affected by the slow flow rate and high flow rate, respectively, as shown in Fig. 4b. Several locations of the low (n = 3) and high (n = 3) staining signal bands were considered for the analysis. It is evident that with slower flow rates, the differences between the microfluidic gradients are higher, as indicated before in the numerical analysis (Fig. 4a) and this leads to higher differences between the neighboring tissue spots. Moreover, with a low flow rate of 300 μl min^{-1}, but with increasing the incubation time from 1 to 2 and 4 min, the differences between the adjacent tissue bands tend to be less (low/high bands intensity signal increases on average from 67% at 1 min to 84% at 4 min for both markers). This can help in decreasing the non-homogeneity in the tissue section staining but at the cost of increasing the incubation time. On the other hand, higher flow rates are capable of dispensing the fluid while rapidly diminishing the differences between the adjacent microfluidic gradient bands, thus leading to fewer differences in the tissue staining. However, higher flow rates generally require some considerations as explained before such as the need for a high-pressure pump, and very firm sealing of the microfluidic chamber otherwise there is a risk of leakage during the experiment, and the associated high tangential shear stress acting on the biological samples being diagnosed. Finally, Fig. 4c shows the effect of the acoustofluidic mixing on diminishing the microfluidic staining gradients for the most non-homogenous experimental settings (300 μl min^{-1} and 1 min of incubation time). The Her2 signal shows a low/high fluorescence intensity larger than a unity, which can be from the uneven spatial distribution of target epitopes on cells. This shows the clear potential of using acoustofluidic mixing for experiments that require low-pressure pumps or are prone to a potential microfluidic leakage or prone to adverse effects on the tissue or cells due to the high shear stress associated with high flow rates.

Acoustofluidics enabling faster immunostaining

Microfluidic systems may suffer from the laminar flow regime, where the fluid travels in infinitesimal parallel layers without eddies, swirls, or any disruption between the fluidic layers and thus mixing may solely proceed through diffusion. The molecular diffusion in a static fluid is the main mechanism of transport in microfluidic systems, which relies on several factors including the inverse of the particle radius.[42] This means that particles or reagent molecules with larger sizes have lower diffusion coefficients, leading to possibly very slow diffusional transport in microfluidic systems. Biological reagents have diffusion coefficients in the range of 10^{-11} to 10^{-12} (m^2 s^{-1}), which means they would need a long time to diffuse across a microfluidic chamber. The implication of this limited transport can be highly adverse on the duration of microfluidic immunoassays, as explained later. Fig. 5a shows a time series of the chamber cross-section, as indicated by the dashed-blue line box in Fig. 1e, showing by numerical simulation the development of

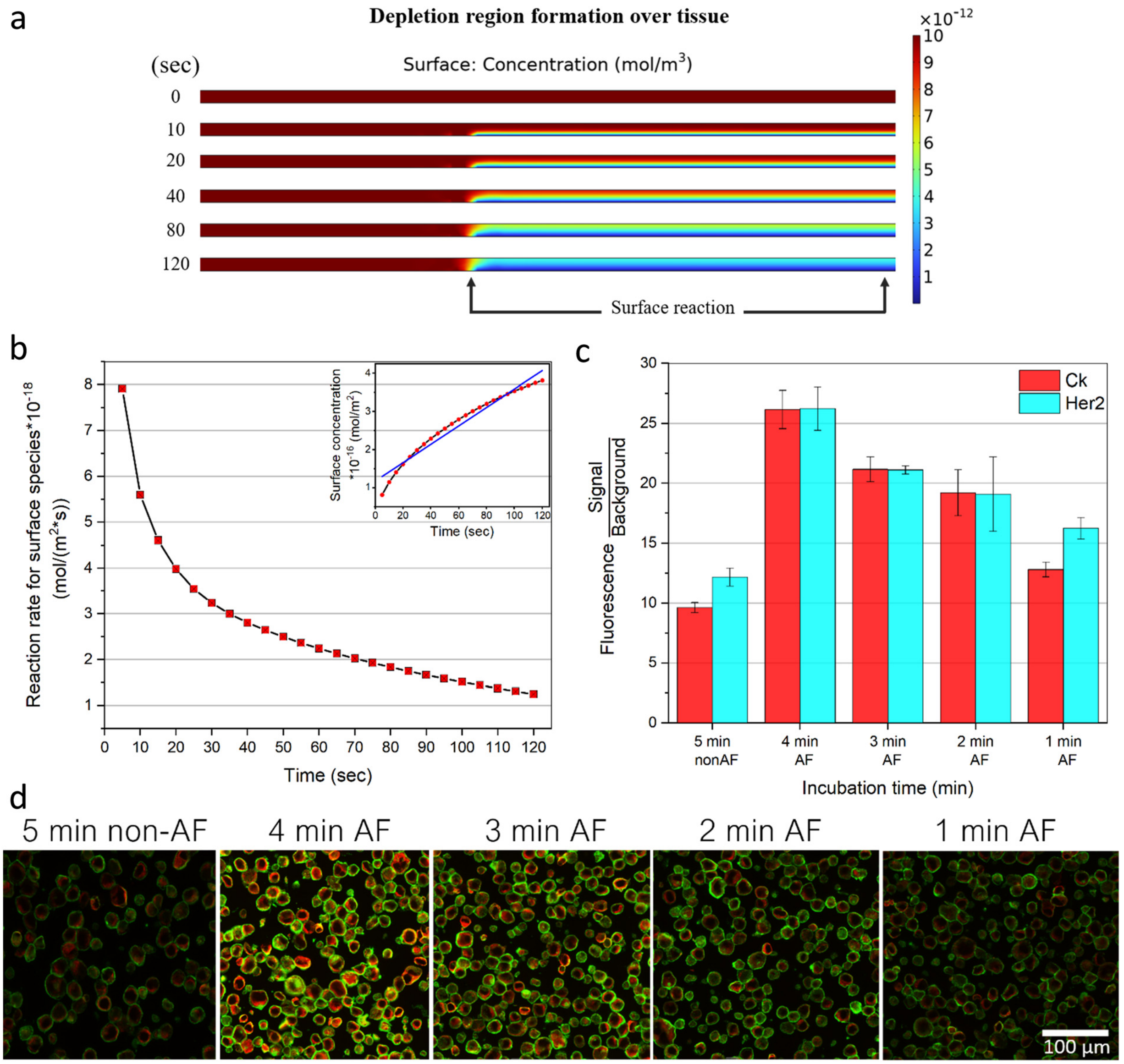

Fig. 5 Reagent concentration depletion region near a reacting surface and acoustofluidic-enhanced immunostaining. (a) Time series images (0 to 120 s) of the chamber cross section (indicated by the dashed-blue line box in Fig. 1e) showing the reagent concentration depletion over the reacting surface tissue. The initial reagent concentration is 10^{-11} (mol m^{-3}) simulated in a microfluidic chamber (17 × 17 × 0.05 mm^3), with a static incubation (no fluid dispensing). (b) The reaction rate (mol m^{-2} s^{-1}) of the surface species during the incubation time of 120 s, corresponding to Fig. 5a. The inset plot of Fig. 5b shows the non-linear increase in the surface reacting species (mol m^{-2}) over the 120 s incubation time. (c) Signal/background experimental fluorescence analysis of the Her2 and CK markers on the Bt-474 cancer cells, for 5 min incubation time without acoustofluidic (non-AF) mixing and 4–1 min incubation time with acoustofluidic (AF) mixing. Error bars represent the standard deviation (n = 3). (d) Fluorescence microscopic images of Bt-474 cancer cells showing the Her2 (green) and CK (red) signals at the different experimental conditions; 5 min incubation time without acoustofluidic (non-AF) mixing and 4–1 min incubation time with acoustofluidic (AF) mixing.

the depletion region over the reacting tissue. At the beginning of the immunoassay incubation time, the reacting tissue surface starts to consume the available reagents in the volumetric vicinity of the tissue and thus the concentration of the available reagents starts to drop. After that, the immunoreaction starts to be limited to the slow diffusion of the reagents to be able to reach the reacting surface. Fig. 5b shows the reaction kinetics of the reacting tissue surface (shown in Fig. 5a with a static incubation), where the inset plot of the Fig. 5b shows the non-linear increase in the surface reacting species concentration (mol m^{-2}) over the incubation time. Fig. 5b shows the change in the reaction rate of the adsorbing species over the incubation time. It shows that the reaction rate decays rapidly even in the first 20 s of the reaction, dropping to 50% of the initial reaction rate. The rate further decays to 25% after 70 s and later to 12.5% after 120 s. Here we simulated a reacting surface with a large available density of sites (3.3×10^{-8} mol m^{-2}) to ensure that the reacting surface is not reaching any saturation during the simulated incubation time. The surface adsorbed concentration after 120 s is still as low as 3.7×10^{-16} mol m^{-2}. A hypothetical reaction that is not limited by the diffusion transport would show a non-decaying reaction rate. This observed decrease clearly shows the effect of the slow diffusion transport of the bioreagents on the microfluidic immunoassay kinetics. Several microfluidic mixing methods in literature have been utilized to reduce this limitation, and have been shown to enhance the reaction rate as explained before. Here, we have utilized acoustofluidic mixing to counteract this diffusion-limited transport for the immunostaining on the Bt-474 cancer cells. Several immunostaining experiments were conducted with different incubation times of the primary and secondary antibodies, as explained before, all at a 1 : 200 dilution ratio. After the sections were stained and mounted for imaging, the signal and background values were analysed, as explained in the ESI.† A 5 min incubation time of each antibody mixture was tested without the acoustofluidic (non-AF) mixing while, incubation times of 4–1 min with the acoustofluidic (AF) mixing were tested, with each of the above conditions repeated ($n = 3$) to ensure the reproducibility of the observed effects. In general, given the rapidly decaying reaction rate observed in Fig. 5b, shortening the incubation time is expected to reduce the achieved reaction signal by a large factor. The surface reacting species concentration shown in the inset plot of Fig. 5b shows that the signal would decrease from 3.7×10^{-16} to 1.9×10^{-16} mol m^{-2} if the incubation time is shortened from 2 to 1 min. However, one sees in Fig. 5c that, even with shortening the incubation times down by 80% with the active actuation of the piezoelectric transducers, the acoustofluidic mixing is capable of rapidly replenishing the bioreagents over the reacting tissue. We have found that the acoustofluidic mixing with shorter incubation times is not only capable of sustaining the immuno-fluorescence signal, but it further provides higher signals. With the shortest incubation time of 1 min, on average, 25% of the Her2 and CK signals were achieved higher than the 5 min incubation time without acoustofluidic mixing. This shows the potential of using the acoustofluidic mixing to shorten the immunostaining incubation times, while still achieving higher signal-to-noise ratios. It is worth noting that the increase in the percentage average of the immuno-fluorescence signal with the acoustofluidic from 1 to 4 min over the 5 min static incubation, is lower with the Her2 marker than with the CK. Several factors can lead to this observation, such as the number of the protein epitopes available on the cells for each marker, but it is worth considering that the Her2 receptors are embedded and highly localized in the cellular membrane,[77] while the CK are mainly found on the cytoplasm and nucleus.[78] This can potentially show the effect of the microfluidic mixing on the enhancement of the cellular markers that are localized more inside the cells than those on the outside membrane. A similar observation is made with the acoustofluidic mixing at different reagents concentration. Finally, Fig. 5d shows the immunofluorescent staining of the Bt-474 cancer cell sections at the different experimental conditions of 5 min incubation times without acoustofluidic mixing, and 4, 3, 2, and 1 min min incubation times with acoustofluidic mixing. A higher and sharper signal is observed for both the Her2 (green color) membranous marker and the CK (red color) cytoplasmic markers.

Acoustofluidics enabling immunostaining with lower reagents consumption

The concentration of the biological reagents (antibodies, DNA, proteins, aptamers, *etc.*) used in an immunoassay is an important factor, since these molecules are generally expensive. A high concentration would result in a higher signal, as long as it doesn't adversely affect the immunoassay performance, for example, due to steric repulsion or increasing the non-specific signal, however, that adds a high cost to the analysis. Fig. 6a shows the simulation results of the surface concentration achieved after 4 min of incubation time at four different reagent concentrations (dilutions) from 10^{-10} to 0.25×10^{-10} mol m^{-3}. It shows clearly that, with a higher initial reagent concentration in the chamber, a higher signal (without reaching surface saturation) is achieved after the same incubation time, while the other lower concentrations (50%, 66.67%, and 75% less concentration than 10^{-10} mol m^{-3}) showed much lower surface concentrations, scaling nearly with the same dilution percentages. This is mainly due to the high abundance of the bioreagents in the vicinity of the reacting surface (tissue) when using high concentrations. Thus, within the same incubation time, there is a higher limitation imposed on the immunoassay reaction with lower concentrations of the bioreagents due to the scarcity of the bioreagents and the slow diffusional transport. It is noteworthy that normalizing the reaction rates of each of the four different simulated concentrations to the initial concentration of the reacting reagents, shows an equal value for all of the four different concentrations at the same time (ESI† Fig. S2). This indicates that the change in the reaction rate over the incubation time is not affected by the concentration used and that the system is highly affected by the diffusional limited transport of the reacting reagents, as explained before. Therefore, acoustofluidic mixing can be a helpful tool here too to mix and replenish the fluid containing the bioreagents over the reacting surface. Fig. 6b shows the experimental analysis (signal/background fluorescence signal) of the Bt-474 cancer cell pellet sections, immune-stained with the Her2 and CK markers, with 4 min incubation times of the different dilution ratios of the primary and secondary antibodies. A dilution ratio of 1 : 100 was tested without the acoustofluidic mixing, and dilution ratios of 1 : 200 (same test as done in Fig. 5d-4 min AF), 1 : 300, and 1 : 400 were tested with the acoustofluidic mixing. As clearly seen, and contrary to what might be expected if a static incubation is used, going to higher dilutions of the primary and secondary antibodies with the acoustofluidic mixing achieved a higher signal over

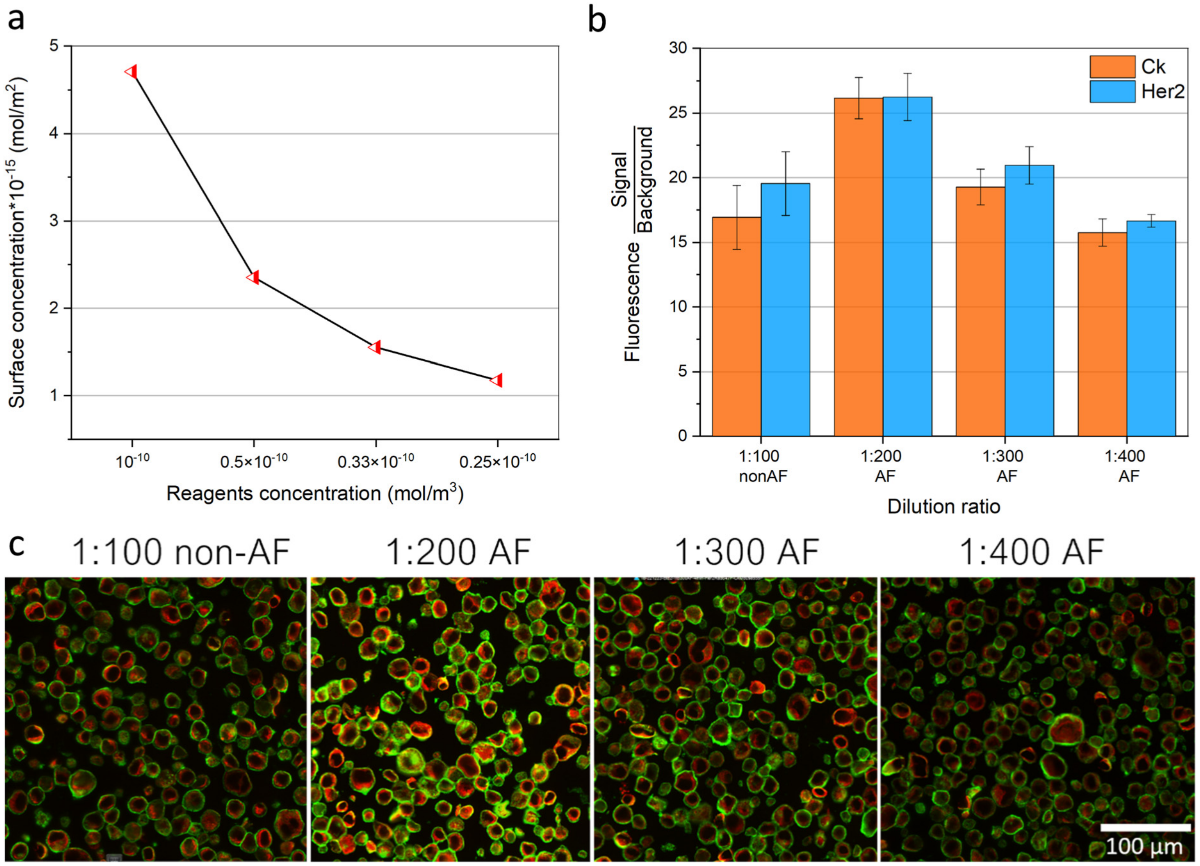

Fig. 6 Acoustofluidic enhanced immunostaining resulting in lower reagents consumption. (a) Simulation of the surface reacting species concentration (mol m^{-2}) obtained after 4 min using different initial reagents concentrations of 10^{-10}, 0.5 × 10^{-10}, 0.33 × 10^{-10}, 0.25 × 10^{-10} mol m^{-3} inside the chamber shown in Fig. 5a. (b) The signal/background experimental fluorescence analysis of the Her2 and CK markers on the Bt-474 cancer cells, at 1:100 antibodies dilution rate without acoustofluidic (non-AF) mixing and at 1:200, 1:300, and 1:400 antibodies dilution rates with acoustofluidic (AF) mixing, all with 4 min of incubation time. Error bars represent the standard deviation (n = 3). (c) Fluorescence microscopic images of Bt-474 cancer cells showing the Her2 (green) and CK (red) signals at the different experimental conditions; 1:100 antibodies dilution rate without acoustofluidic (non-AF) mixing and at 1:200, 1:300, and 1:400 antibodies dilution rates with acoustofluidic (AF) mixing, all with 4 min of incubation time.

the more concentrated antibodies but with a static incubation. Analogous to the reduction in the incubation time with the acoustofluidic mixing before, reducing the antibodies consumption by 50% and 66.6% with the acoustofluidic mixing not only reduces the experimental cost but also provides a higher signal-to-background ratio. 1:200 and 1:300 dilution rates with the acoustofluidic mixing showed an increase in the signals by 35% in CK and 12% in Her2 and 25% in CK and 6% in Her2, respectively, over the 1:100 dilution rate without the acoustofluidic mixing. However, a 1:400 dilution rate with the acoustofluidic mixing resulted in lower signals (7% in CK and 17% in Her2). Finally, Fig. 6c shows the immunofluorescent images of the Bt-474 cell pellet sections at the different antibodies' dilution ratios of 1:100 without the acoustofluidic mixing, and 1:200, 1:300, and 1:400 with the acoustofluidic mixing. A higher signal is observed for Her2 and CK markers even with the 1:200 and 1:300 dilution rate of the antibodies when the acoustofluidic mixing is used. This shows the possibility of using acoustofluidic mixing to achieve higher immunoassay signal-to-noise ratios while consuming lower volumes of the expensive bioreagents.

Conclusions

We have investigated the integration of acoustofluidic streaming for microfluidic mixing and for enhancing microfluidic immunostaining for cancer diagnostics. Piezoelectric elements mounted close to the microfluidic chamber were capable of inducing large-scale acoustic streaming vortex-like patterns. Numerical simulation was conducted to explain the working concept of the acoustofluidic mixing in microfluidic systems. After that, the possibility of obtaining non-homogenous staining of the tumor tissues using a microfluidic chip with network channel design at low fluidic flow rates was investigated by simulation and experiments. Additionally, we have elaborated by numerical simulation on how the shorter incubation times and the lower reagent concentrations, and their diffusion-limited transport inside microfluidic systems can be an obstacle against the enhancement of the microfluidic immunoassay performance. Finally, acoustofluidic mixing was used for improving the immunostaining of Her2 and CK markers on Bt-474 cancel cell pellet sections. Acoustofluidic mixing was capable of providing homogeneous and uniform staining, even at conditions that would generate a very sharp concentration and staining gradients at static incubation. Moreover, acoustofluidic mixing further enhanced the immunostaining performance by reducing the regent incubation time by 80% and the reagent concentration by 66%, while obtaining a higher signal than with static incubation. The reported method therefore can serve as a good approach for obtaining faster and cost-effective diagnostic assays in microfluidic systems.

Author contributions

Conceptualization: M. S. D., simulation: M. S. D., experimental investigation: M. S. D., data curation: M. S. D., visualization: M. S. D., writing – original draft: M. S. D., editing: M. S. D., D. D., M. A. M. G., supervision: D. D., M. A. M. G.

Conflicts of interest

There are no conflicts to declare.

Acknowledgements

This project has received funding from the European Union's Horizon 2020 research and innovation programme under the Marie Skłodowska-Curie grant agreement No. 754354.

Notes and references

1 C. Rivet, H. Lee, A. Hirsch, S. Hamilton and H. Lu, Microfluidics for medical diagnostics and biosensors, *Chem. Eng. Sci.*, 2011, **66**, 1490–1507.

2 W. G. Lee, Y. G. Kim, B. G. Chung, U. Demirci and A. Khademhosseini, Nano/Microfluidics for diagnosis of infectious diseases in developing countries, *Adv. Drug Delivery Rev.*, 2010, **62**, 449–457.

3 J. L. Garcia-Cordero and S. J. Maerkl, Microfluidic systems for cancer diagnostics, *Curr. Opin. Biotechnol.*, 2020, **65**, 37–44.

4 K. S. Elvira, X. C. i Solvas, R. C. R. Wootton and A. J. deMello, The past, present and potential for microfluidic reactor technology in chemical synthesis, *Nat. Chem.*, 2013, **5**, 905–915.

5 P. S. Dittrich and A. Manz, Lab-on-a-chip: microfluidics in drug discovery, *Nat. Rev. Drug Discovery*, 2006, **5**, 210–218.

6 B. Bruijns, A. Van Asten, R. Tiggelaar and H. Gardeniers, Microfluidic Devices for Forensic DNA Analysis: A Review, *Biosensors*, 2016, **6**, 41.

7 E. R. Choban, L. J. Markoski, A. Wieckowski and P. J. A. Kenis, Microfluidic fuel cell based on laminar flow, *J. Power Sources*, 2004, **128**, 54–60.

8 Y. Lin, D. Gritsenko, S. Feng, Y. C. Teh, X. Lu and J. Xu, Detection of heavy metal by paper-based microfluidics, *Biosens. Bioelectron.*, 2016, **83**, 256–266.

9 S. Halldorsson, E. Lucumi, R. Gómez-Sjöberg and R. M. T. Fleming, Advantages and challenges of microfluidic cell culture in polydimethylsiloxane devices, *Biosens. Bioelectron.*, 2015, **63**, 218–231.

10 A. M. Streets and Y. Huang, Chip in a lab: Microfluidics for next generation life science research, *Biomicrofluidics*, 2013, **7**, 011302.

11 C. Chen, B. T. Mehl, A. S. Munshi, A. D. Townsend, D. M. Spence and R. Scott Martin, 3D-printed microfluidic devices: fabrication, advantages and limitations—a mini review, *Anal. Methods*, 2016, **8**, 6005–6012.

12 Y. Liu and X. Jiang, Why microfluidics? Merits and trends in chemical synthesis, *Lab Chip*, 2017, **17**, 3960–3978.

13 D. T. Chiu, A. J. deMello, D. Di Carlo, P. S. Doyle, C. Hansen and R. M. Maceiczyk, *et al.*, Small but Perfectly Formed? Successes, Challenges, and Opportunities for Microfluidics in the Chemical and Biological Sciences, *Chem*, 2017, **2**, 201–223.

14 S. Kwon, C. H. Cho, Y. Kwon, E. S. Lee and J. K. Park, A Microfluidic Immunostaining System Enables Quality Assured and Standardized Immunohistochemical Biomarker Analysis, *Sci. Rep.*, 2017, **7**, 45968.

15 D. Migliozzi, B. Pelz, D. G. Dupouy, A. L. Leblond, A. Soltermann and M. A. M. Gijs, Microfluidics-assisted multiplexed biomarker detection for in situ mapping of immune cells in tumor sections, *Microsyst. Nanoeng.*, 2019, **5**, 1–12.

16 D. G. Dupouy, A. T. Ciftlik, M. Fiche, D. Heintze, B. Bisig and L. de Leval, *et al.*, Continuous quantification of HER2 expression by microfluidic precision immunofluorescence estimates HER2 gene amplification in breast cancer, *Sci. Rep.*, 2016, **6**, 20277.

17 L. F. Horowitz, A. D. Rodriguez, T. Ray and A. Folch, Microfluidics for interrogating live intact tissues, *Microsyst. Nanoeng.*, 2020, **6**, 1–27.

18 T. M. Grabinski, A. Kneynsberg, F. P. Manfredsson and N. M. Kanaan, A Method for Combining RNAscope In Situ Hybridization with Immunohistochemistry in Thick Free-Floating Brain Sections and Primary Neuronal Cultures, *PLoS One*, 2015, **10**, e0120120.

19 A. T. Ciftlik, H. A. Lehr and M. A. M. Gijs, Microfluidic processor allows rapid HER2 immunohistochemistry of breast carcinomas and significantly reduces ambiguous (2+) read-outs, *Proc. Natl. Acad. Sci. U. S. A.*, 2013, **110**, 5363–5368.

20 H. A. Alturkistani, F. M. Tashkandi and Z. M. Mohammedsaleh, Histological Stains: A Literature Review and Case Study, *Glob. J. Health Sci.*, 2016, **8**, 72–79.

21 J. Kohl, J. Ng, S. Cachero, E. Ciabatti, M. J. Dolan and B. Sutcliffe, *et al.*, Ultrafast tissue staining with chemical tags, *Proc. Natl. Acad. Sci. U. S. A.*, 2014, **111**, E3805-14.

22 H. T. Nguyen, D. Migliozzi, B. Bisig, L. de Leval and M. A. M. Gijs, High-content, cell-by-cell assessment of HER2 overexpression and amplification: a tool for intratumoral heterogeneity detection in breast cancer, *Lab. Invest.*, 2019, **99**, 722–732.

23 S. Brajkovic, B. Pelz, M. G. Procopio, A. L. Leblond, G. Repond and A. Schaub-Clerigué, *et al.*, Microfluidics-based immunofluorescence for fast staining of ALK in lung adenocarcinoma, *Diagn. Pathol.*, 2018, **13**, 79.

24 S. Brajkovic, D. G. Dupouy, L. de Leval and M. A. Gijs, Microfluidics for rapid cytokeratin immunohistochemical staining in frozen sections, *Lab. Invest.*, 2017, **97**, 983–991.

25 N. Maïno, T. Hauling, G. Cappi, N. Madaboosi, D. G. Dupouy and M. Nilsson, A microfluidic platform towards automated multiplexed in situ sequencing, *Sci. Rep.*, 2019, **9**, 3542.

26 G. Cappi, D. G. Dupouy, M. A. Comino and A. T. Ciftlik, Ultra-fast and automated immunohistofluorescent multistaining using a microfluidic tissue processor, *Sci. Rep.*, 2019, **9**, 4489.

27 G. A. Cooksey, C. G. Sip and A. Folch, A multi-purpose microfluidic perfusion system with combinatorial choice of inputs, mixtures, gradient patterns, and flow rates, *Lab Chip*, 2009, **9**, 417–426.

28 E. Berthier and D. J. Beebe, Gradient generation platforms: new directions for an established microfluidic technology, *Lab Chip*, 2014, **14**, 3241–3247.

29 A. E. Kamholz, B. H. Weigl, B. A. Finlayson and P. Yager, Quantitative Analysis of Molecular Interaction in a Microfluidic Channel: The T-Sensor, *Anal. Chem.*, 1999, **71**, 5340–5347.

30 N. L. Jeon, S. K. W. Dertinger, D. T. Chiu, I. S. Choi, A. D. Stroock and G. M. Whitesides, Generation of Solution and Surface Gradients Using Microfluidic Systems, *Langmuir*, 2000, **16**, 8311–8316.

31 G. M. Walker, J. Sai, A. Richmond, M. Stremler, C. Y. Chung and J. P. Wikswo, Effects of flow and diffusion on chemotaxis studies in a microfabricated gradient generator, *Lab Chip*, 2005, **5**, 611–618.

32 B. G. Chung, L. A. Flanagan, S. W. Rhee, P. H. Schwartz, A. P. Lee and E. S. Monuki, *et al.*, Human neural stem cell growth and differentiation in a gradient-generating microfluidic device, *Lab Chip*, 2005, **5**, 401–406.

33 S. Paliwal, P. A. Iglesias, K. Campbell, Z. Hilioti, A. Groisman and A. Levchenko, MAPK-mediated bimodal gene expression and adaptive gradient sensing in yeast, *Nature*, 2007, **446**, 46–51.

34 S. K. W. Dertinger, X. Jiang, Z. Li, V. N. Murthy and G. M. Whitesides, Gradients of substrate-bound laminin orient axonal specification of neurons, *Proc. Natl. Acad. Sci. U. S. A.*, 2002, **99**, 12542–12547.

35 V. Silverio, S. Guha, A. Keiser, R. Natu, D. R. Reyes and H. van Heeren, *et al.*, Overcoming technological barriers in microfluidics: Leakage testing, *Front. Bioeng. Biotechnol.*, 2022, **10**, DOI: 10.3389/fbioe.2022.958582.

36 S. Ogden, R. Bodén and K. Hjort, A Latchable Valve for High-Pressure Microfluidics, *J. Microelectromech. Syst.*, 2010, **19**, 396–401.

37 S. Naskar, V. Kumaran and B. Basu, Reprogramming the Stem Cell Behavior by Shear Stress and Electric Field Stimulation: Lab-on-a-Chip Based Biomicrofluidics in Regenerative Medicine, *Regener. Eng. Transl. Med.*, 2019, **5**, 99–127.

38 V. K. Sidhaye, K. S. Schweitzer, M. J. Caterina, L. Shimoda and L. S. King, Shear stress regulates aquaporin-5 and airway epithelial barrier function, *Proc. Natl. Acad. Sci. U. S. A.*, 2008, **105**, 3345–3350.

39 B. Liu, J. Zhao and J. Qian, Numerical analysis of cavitation erosion and particle erosion in butterfly valve, *Eng. Failure Anal.*, 2017, **80**, 312–324.

40 X. Liu, Z. Wu, B. Li, J. Zhao, J. He and W. Li, *et al.*, Influence of inlet pressure on cavitation characteristics in regulating valve, *Eng. Appl. Comput. Fluid Mech.*, 2020, **14**, 299–310.

41 K. Katoh, Rapid fixation and immunofluorescent staining of cultured cells using microwave irradiation, *J. Histotechnol.*, 2011, **34**, 29–34.

42 M. S. Draz, K. Uning, D. Dupouy and M. A. M. Gijs, Efficient AC electrothermal flow (ACET) on-chip for enhanced immunoassays, *Lab Chip*, 2023, **23**, 1637–1648.

43 M. Sigurdson, D. Wang and C. D. Meinhart, Electrothermal stirring for heterogeneous immunoassays, *Lab Chip*, 2005, **5**, 1366–1373.

44 W. M. Saltzman, M. L. Radomsky, K. J. Whaley and R. A. Cone, Antibody diffusion in human cervical mucus, *Biophys. J.*, 1994, **66**, 508–515.

45 G. L. Lukacs, P. Haggie, O. Seksek, D. Lechardeur, N. Freedman and A. S. Verkman, Size-dependent DNA Mobility in Cytoplasm and Nucleus, *J. Biol. Chem.*, 2000, **275**, 1625–1629.

46 S. Magaki, S. A. Hojat, B. Wei, A. So and W. H. Yong, An Introduction to the Performance of Immunohistochemistry, in *Biobanking: Methods and Protocols*, ed. W. H. Yong, Methods in Molecular Biology, Springer, New York, NY, 2019, pp. 289–298, DOI: 10.1007/978-1-4939-8935-5_25.

47 G. E. Hoffman, K. J. Murphy and L. V. Sita, The Importance of Titrating Antibodies for Immunocytochemical Methods, *Curr. Protoc. Neurosci.*, 2016, **76**, 2.12.1–2.12.37.

48 S. H. Lee, D. van Noort, J. Y. Lee, B. T. Zhang and T. H. Park, Effective mixing in a microfluidic chip using magnetic particles, *Lab Chip*, 2009, **9**, 479–482.

49 E. S. Shanko, Y. van de Burgt, P. D. Anderson and J. M. J. den Toonder, Microfluidic Magnetic Mixing at Low Reynolds Numbers and in Stagnant Fluids, *Micromachines*, 2019, **10**, 731.

50 X. Chen, Y. Ning, S. Pan, B. Liu, Y. Chang and W. Pang, *et al.*, Mixing during Trapping Enabled a Continuous-Flow Microfluidic Smartphone Immunoassay Using Acoustic Streaming, *ACS Sens.*, 2021, **6**, 2386–2394.

51 P. Zhang, H. Bachman, A. Ozcelik and T. J. Huang, Acoustic Microfluidics, *Annu. Rev. Anal. Chem.*, 2020, **13**, 17–43.

52 J. Rufo, F. Cai, J. Friend, M. Wiklund and T. J. Huang, Acoustofluidics for biomedical applications, *Nat. Rev. Methods Primers*, 2022, **2**, 1–21.

53 H. V. Phan, M. B. Coşkun, M. Şeşen, G. Pandraud, A. Neild and T. Alan, Vibrating membrane with discontinuities for rapid and efficient microfluidic mixing, *Lab Chip*, 2015, **15**, 4206–4216.

54 H. Bachman, C. Chen, J. Rufo, S. Zhao, S. Yang and Z. Tian, *et al.*, An acoustofluidic device for efficient mixing over a wide range of flow rates, *Lab Chip*, 2020, **20**, 1238–1248.

55 A. Ozcelik, D. Ahmed, Y. Xie, N. Nama, Z. Qu and A. A. Nawaz, *et al.*, An Acoustofluidic Micromixer via Bubble Inception and Cavitation from Microchannel Sidewalls, *Anal. Chem.*, 2014, **86**, 5083–5088.

56 R. H. Liu, R. Lenigk, R. L. Druyor-Sanchez, J. Yang and P. Grodzinski, Hybridization Enhancement Using Cavitation Microstreaming, *Anal. Chem.*, 2003, **75**, 1911–1917.

57 C. Y. Lee, C. L. Chang, Y. N. Wang and L. M. Fu, Microfluidic Mixing: A Review, *Int. J. Mol. Sci.*, 2011, **12**, 3263–3287.

58 W. Y. Ng, S. Goh, Y. C. Lam, C. Yang and I. Rodríguez, DC-biased AC-electroosmotic and AC-electrothermal flow mixing in microchannels, *Lab Chip*, 2009, **9**, 802–809.

59 M. L. Y. Sin, V. Gau, J. C. Liao and P. K. Wong, Electrothermal Fluid Manipulation of High-Conductivity Samples for Laboratory Automation Applications, *JALA*, 2010, **15**, 426–432.

60 A. G. Waks and E. P. Winer, Breast Cancer Treatment: A Review, *JAMA, J. Am. Med. Assoc.*, 2019, **321**, 288–300.

61 M. M. Shao, S. K. Chan, A. M. C. Yu, C. C. F. Lam, J. Y. S. Tsang and P. C. W. Lui, *et al.*, Keratin expression in breast cancers, *Virchows Arch.*, 2012, **461**, 313–322.

62 I. Langmuir, The adsorption of gases on plane surfaces of glass, mica and platinum, *J. Am. Chem. Soc.*, 1918, **40**, 1361–1403.

63 W. J. Parnell and R. De Pascalis, Soft metamaterials with dynamic viscoelastic functionality tuned by pre-deformation, *Philos. Trans. R. Soc., A*, 2019, **377**, 20180072.

64 F. Xin and T. Lu, Tensional acoustomechanical soft metamaterials, *Sci. Rep.*, 2016, **6**, 27432.

65 J. Dual and T. Schwarz, Acoustofluidics 3: Continuum mechanics for ultrasonic particle manipulation, *Lab Chip*, 2011, **12**, 244–252.

66 A. Aghakhani, H. Cetin, P. Erkoc, G. I. Tombak and M. Sitti, Flexural wave-based soft attractor walls for trapping microparticles and cells, *Lab Chip*, 2021, **21**, 582–596.

67 P. B. Muller, R. Barnkob, M. J. H. Jensen and H. Bruus, A numerical study of microparticle acoustophoresis driven by acoustic radiation forces and streaming-induced drag forces, *Lab Chip*, 2012, **12**, 4617–4627.

68 M. Wiklund, R. Green and M. Ohlin, Acoustofluidics 14: Applications of acoustic streaming in microfluidic devices, *Lab Chip*, 2012, **12**, 2438–2451.

69 S. J. Lighthill, Acoustic streaming, *J. Sound Vib.*, 1978, **61**, 391–418.

70 J. Wu, Acoustic Streaming and Its Applications, *Fluids*, 2018, **3**, 108.

71 K. Shahzad, W. V. Aeken, M. Mottaghi, V. K. Kamyab and S. Kuhn, Aggregation and clogging phenomena of rigid microparticles in microfluidics, *Microfluid. Nanofluid.*, 2018, **22**, 104.

72 W. L. Nyborg, Acoustic Streaming near a Boundary, *J. Acoust. Soc. Am.*, 1958, **30**, 329–339.

73 S. Deng, K. Jia, E. Wu, X. Hu, Z. Fan and K. Yang, Controllable Micro-Particle Rotation and Transportation Using Sound Field Synthesis Technique, *Appl. Sci.*, 2018, **8**, 73.

74 A. Lamprecht, T. Schwarz, J. Wang and J. Dual, Viscous torque on spherical micro particles in two orthogonal acoustic standing wave fields, *J. Acoust. Soc. Am.*, 2015, **138**, 23–32.

75 J. S. Bach and H. Bruus, Theory of pressure acoustics with viscous boundary layers and streaming in curved elastic cavities, *J. Acoust. Soc. Am.*, 2018, **144**, 766–784.

76 R. Barnkob, P. Augustsson, T. Laurell and H. Bruus, Acoustic radiation- and streaming-induced microparticle velocities determined by microparticle image velocimetry in an ultrasound symmetry plane, *Phys. Rev. E: Stat., Nonlinear, Soft Matter Phys.*, 2012, **86**, 056307.

77 C. A. Hudis, Trastuzumab — Mechanism of Action and Use in Clinical Practice, *N. Engl. J. Med.*, 2007, **357**, 39–51.

78 V. Barak, H. Goike, K. W. Panaretakis and R. Einarsson, Clinical utility of cytokeratins as tumor markers, *Clin. Biochem.*, 2004, **37**, 529–540.